Sheng, Yufei; Hu, Yue; Fan, Zheyong; Bao, Hua

Size effect and transient phonon transport mechanism in approach-to-equilibrium molecular dynamics simulations

Published in:
Physical Review B

DOI:
10.1103/PhysRevB.105.075301

Published: 15/02/2022

Document Version
Publisher's PDF, also known as Version of record

Please cite the original version:
Sheng, Y., Hu, Y., Fan, Z., & Bao, H. (2022). Size effect and transient phonon transport mechanism in approach-to-equilibrium molecular dynamics simulations. *Physical Review B*, *105*(7), 1-8. Article 075301. https://doi.org/10.1103/PhysRevB.105.075301

Size effect and transient phonon transport mechanism in approach-to-equilibrium molecular dynamics simulations

Yufei Sheng [1,*] Yue Hu,[1,*] Zheyong Fan,[2] and Hua Bao [1,†]
[1]*University of Michigan–Shanghai Jiao Tong University Joint Institute, Shanghai Jiao Tong University, Shanghai 200240, People's Republic of China*
[2]*QTF Centre of Excellence, Department of Applied Physics, Aalto University, FI-00076 Aalto, Finland*

(Received 11 November 2021; revised 22 January 2022; accepted 24 January 2022; published 7 February 2022)

Approach-to-equilibrium molecular dynamics (AEMD) is a widely used molecular dynamics (MD) method to extract thermal transport properties in different material systems. Despite the success in many applications, the thermal transport mechanism in AEMD is not well understood. Although AEMD can simulate larger domain than other MD variants, it still suffers from simulation domain size effect. In addition, the size effect is quite different from that of the nonequilibrium molecular dynamics (NEMD) simulations. In this paper, we reveal the phonon transport mechanism in AEMD by comparing the size-dependent thermal conductivity values of AEMD and phonon Boltzmann transport equation. We show that the simulation size of AEMD should be defined as half of the size in the conventional AEMD simulations with periodic boundary conditions. Also, the size effect in AEMD originates from ballistic phonon transport. Different from NEMD, some phonons with long mean-free paths do not contribute to the thermal conductivity, resulting in a smaller thermal conductivity than NEMD with the same size. Based on the phonon transport mechanism in AEMD, we suggest an extrapolation method for AEMD to obtain bulk thermal conductivity.

DOI: 10.1103/PhysRevB.105.075301

I. INTRODUCTION

Molecular dynamics (MD) is a widely used atomistic simulation method for the investigation of nanoscale thermal transport [1–10]. Several MD methods have been developed to simulate thermal transport process in the past few decades, including equilibrium molecular dynamics (EMD) [11–14], and nonequilibrium molecular dynamics (NEMD) [1–3]. EMD is based on the fluctuation-dissipation theorem and the bulk thermal conductivity can be extracted from the heat current autocorrelation function [13–16]. In NEMD, a steady heat flux is established between two thermostats and the thermal conductivity can be directly calculated by Fourier's law [17–21]. The two methods have achieved great success in the atomistic simulation of many material systems [22–28]. However, the computational costs are relatively large [29–31]. Recently, researchers have developed a new MD variant called approach-to-equilibrium molecular dynamics (AEMD) [32] with the advantage of smaller computational cost.

The AEMD method simulates the temperature decay process from a step-difference temperature profile to an equilibrium temperature profile and calculates the transient thermal conductivity based on Fourier's law [32–35], which also corresponds to the process of the thermal transient grating measurement [36–38]. Compared with EMD, the AEMD method has the advantage of smaller oscillations and less uncertainty [39]. Compared with NEMD, the AEMD method has much smaller computational cost for the same length scale, due to its transient nature [32]. AEMD was developed by Lampin *et al.* [32], and was adopted to investigate the thermal conductivity of semiconductors, such as silicon and germanium [32,34]. Subsequently, AEMD was used to calculate thermal conductivity in low-dimensional materials [40,41], thermal resistance at the interfaces [42,43], porous materials [44,45], and polymer chains [46,47]. It is worth mentioning that the maximum size studied using the AEMD method can reach 0.1 mm [41], which is far beyond the limit of other MD-based approaches. The AEMD has also been implemented to work with *ab initio* molecular dynamics [48] and machine-learning potentials [49].

Despite the success in many applications, the thermal transport mechanism in AEMD is still unclear. Similar to EMD and NEMD, AEMD also suffers from simulation domain size effect [32,34]. When the bulk thermal conductivity is of interest, it is usually obtained by extrapolation from the limited size thermal conductivities values [29,30,50]. For EMD and NEMD, there are several recent works that discussed their size effect. For example, Wang *et al.* [31] showed the difference of the size effect in EMD and NEMD. They suggested that the size effect in EMD is due to the limited available long-wavelength phonon modes in the simulation domain as the size decreases, while the size effect in NEMD is attributed to the phonon scattering with the reservoir which cuts off the phonon mean-free paths [20,30]. Subsequently, Dong *et al.* [51] found that the bulk thermal conductivity in EMD can be identical to the extrapolated thermal conductivity in NEMD. They showed that by converting the correlation time to an effective simulation size in EMD,

*These authors contributed equally to this work.
†hua.bao@sjtu.edu.cn

the size-dependent thermal conductivities in the two MD approaches are unified. A recently developed homogeneous nonequilibrium molecular dynamics method [52–55], which is more efficient than EMD, has similar size effect with EMD [56]. Moreover, Hu *et al.* [21] recently have shown that the size-dependent NEMD results are in quantitative agreement with the solution of phonon Boltzmann transport equation (BTE), which indisputably proves that the size effect of NEMD can be fully interpreted with the ballistic phonon transport effect. In comparison, AEMD also has simulation domain size effect [32,34], which is not well understood. Moreover, with the same simulation size, the extracted thermal conductivity of AEMD is quite different from that of NEMD [57].

In this paper, we develop a deeper understanding about AEMD simulation by a detailed comparison of the size-dependent thermal conductivity values of AEMD, NEMD, and the phonon BTE simulations. Through such a comparison, we reveal the phonon transport mechanism in AEMD simulations. We then propose an improved extrapolation method for AEMD to obtain the bulk thermal conductivity from the simulation results of finite-size structures.

The paper is organized as follows. In Sec. II, we calculate the different size-dependent thermal conductivities of crystal silicon in NEMD and AEMD and discover their differences. In Sec. III, we discuss the definition of the simulation domain size in AEMD simulation. In Sec. IV, we reveal the phonon transport mechanism in AEMD by unifying AEMD with transient BTE. In Sec. V, an extrapolation method is proposed to extrapolate bulk thermal conductivity from the AEMD results with limited size. In Sec. VI, we present summaries and conclusions.

II. SIZE-DEPENDENT THERMAL CONDUCTIVITY

In this section, we compare the size-dependent thermal conductivity in AEMD and NEMD, taking silicon with the Tersoff potential [58] as a prototype. All simulations are performed using the LAMMPS package [59].

Following previous works [32,34], a simulation domain with periodic boundary conditions in the x, y, z directions is adopted in AEMD simulations, as shown in Fig. 1(a). The length along the x axis is defined as the characteristic size L. An initial step-difference temperature profile is established, dividing the domain into the hot and cold blocks. During the simulation process, the difference between the average temperatures of the two blocks declines gradually until an equilibrium state is approached [32], as shown in Fig. 1(b). Simulation details of AEMD can be found in Appendix A.

To extract thermal conductivity values from AEMD simulations, the heat diffusion equation based on Fourier's law for the same system is solved. The thermal conductivity can be extracted by fitting the decay curve of the average temperature difference between the hot block and cold block with the solution of the heat diffusion equation,

$$\Delta T(t) = \sum_{m=0}^{\infty} \frac{8(T_1 - T_2)}{(2m+1)^2 \pi^2} e^{-\{[(2m+1)^2 t]/\tau\}}, \tag{1}$$

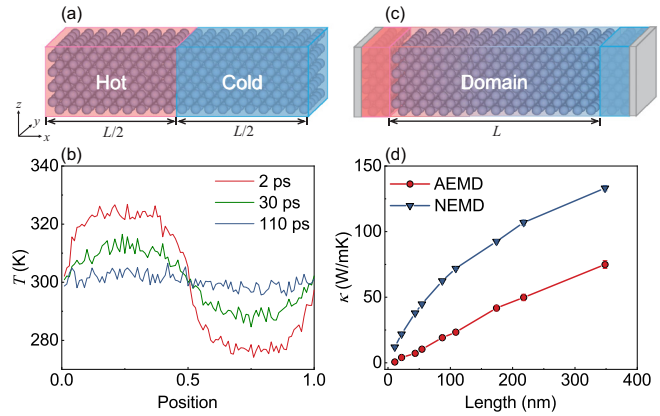

FIG. 1. (a) The simulation domain in AEMD. The domain is divided into two blocks, hot and cold, each block with a size of $L/2$. The initial temperatures of the hot and cold block are 320 and 280 K, respectively. (b) Decay of the temperature profile in AEMD. The length of the domain is 109 nm. Three sample times (2, 30, and 110 ps) are selected to describe the temperature decay process from step difference to equilibrium. (c) The simulation domain in NEMD. The size of the domain is L. Two thermal reservoirs are located on both sides of the domain with 320 and 280 K, respectively. Two layers of atoms are fixed at both ends of the x axis. (d) Comparison of size-dependent thermal conductivity in AEMD and NEMD. The blue triangles represent the NEMD results and the red dots represent the AEMD results. Note that the error bars have comparable size of the markers.

where ΔT is the average temperature difference between the hot block and the cold block, T_1 and T_2 are the initial temperatures in the hot and cold block, and τ is the decay time that is related to the thermal conductivity κ through

$$\kappa = \frac{L^2 C_V}{4\pi^2 \tau}. \tag{2}$$

In Eq. (2), L is the simulation size along the x axis and C_V is the heat capacity per unit volume. Through fitting τ in AEMD simulations, the thermal conductivity value of each sample can be obtained.

To compare with AEMD, NEMD simulations with the same material and different sizes are also carried out. The sample with length L in NEMD is in contact with two thermal reservoirs using the Langevin thermostat [21]. The simulation domain is shown in Fig. 1(c) and the simulation details in NEMD can also be found in Appendix A.

The heat flux can be extracted after establishing a steady state and the thermal conductivity is calculated by $\kappa = \frac{q}{\Delta T/L}$, where q is the heat flux in the x direction, and ΔT is the temperature difference between the two thermal reservoirs. Note that it has been proved that such a definition of thermal conductivity should be used instead of the linear fitting approach [20,21]. The size-dependent thermal conductivity in AEMD and NEMD are represented by red dots and blue triangles, respectively, in Fig. 1(d). The length L of the simulation sample is chosen from 10 to 348 nm. Notable differences can be observed between the size-dependent thermal conductivity of NEMD and AEMD simulations. For sample size $L = 11$ nm, the thermal conductivity in AEMD is 0.64 W/mK, while the

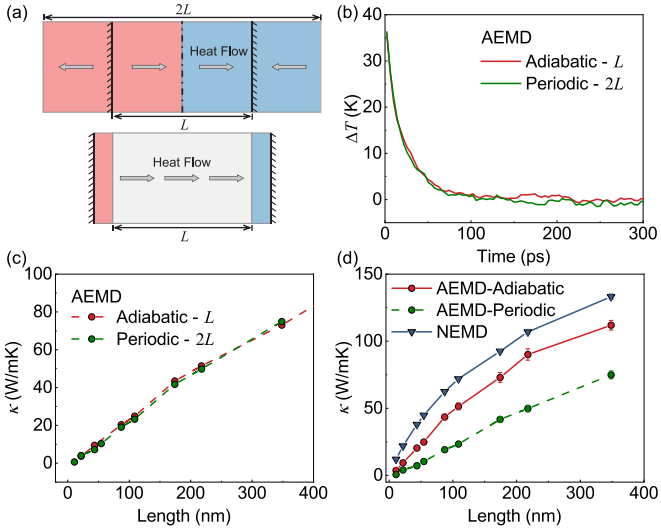

FIG. 2. (a) The direction of heat flow in AEMD and NEMD. For AEMD, in the periodic model with length $2L$, the heat flows are in the forward and reverse directions. In the adiabatic model with length L, the heat flow is only in the forward direction. For NEMD, the heat flow is in the forward direction from the heat source to the heat sink. (b) The decay process of temperature differences between hot and cold blocks in the adiabatic and periodic models. The red line represents the adiabatic model with length L and the green line represents the periodic model with length $2L$. The length L of the domain is 54 nm. (c) Thermal conductivity in the adiabatic and periodic models of AEMD. The red and green dots represent the thermal conductivity in the adiabatic model with length L and in the periodic model with length $2L$. The error bars are very small and thus omitted. (d) Comparison of size-dependent thermal conductivity between NEMD, adiabatic model, and periodic model in AEMD. The blue triangles, red dots, and green dots represent the NEMD results, AEMD results with the adiabatic model, and the periodic model, respectively.

thermal conductivity in NEMD is 12.03 W/mK, around 19× larger than that in AEMD. For $L = 348$ nm, the thermal conductivity in NEMD is about twice as large as that in AEMD.

III. DEFINITION OF THE SIZE

In Sec. II, the boundary conditions in AEMD and NEMD follow the settings of most previous papers [12,21,32,34]. In AEMD, periodic boundary conditions are applied in all directions, while in NEMD, fixed boundary conditions are applied in the direction of heat conduction. Such a setting leads to different heat-flow directions in these two methods. In AEMD, the heat flow is simultaneously transported in the forward and reverse directions of the x axis [Fig. 2(a), the sample of size $2L$]. In NEMD, the heat flow is in the forward direction from the heat source to the heat sink.

Due to the symmetry of the forward and reverse heat flows in AEMD simulations, we can just consider the middle region with length L of the simulation domain, and set the adiabatic boundary conditions by fixing atoms on the boundary, as shown in Fig. 2(a). We later name the original simulation setting with size $2L$ "periodic model" and the one with size L "adiabatic model." To prove the equivalence of periodic model with length $2L$ and the adiabatic model with length L, the AEMD simulations with the same initial conditions are carried out for the two systems, and the results are shown in Fig. 2(b). The decay of the average temperature difference for the two models are almost identical.

To extract the thermal conductivity in the adiabatic model, the heat diffusion equation for the simulation domain is solved. The expression of thermal conductivity in Eq. (2) needs to be modified as

$$\kappa = \frac{L^2 C_V}{\pi^2 \tau'}, \tag{3}$$

where τ' is the decay time in the adiabatic model. The size-dependent thermal conductivity in the adiabatic model is calculated and compared with the periodic model in Fig. 2(c). The nearly identical results further confirm that the adiabatic model with length L is equivalent to the periodic model with length $2L$. It is worth mentioning that applying the fixed boundary in AEMD can reduce computational cost compared to using the periodic boundary, because only half of the simulation domain is needed when identical results are obtained.

We substitute the adiabatic model for the periodic model in AEMD and compare its size-dependent thermal conductivity results with that in NEMD again in Fig. 2(d). The gap between the two methods has narrowed evidently, but is not eliminated. At 11 nm, the thermal conductivity in the adiabatic model of AEMD is 3.69 W/mK. The NEMD result is still about 3× larger than that in AEMD. The relative difference reduces with increasing simulation domain length, but is still notable. These results indicate that there are other differences between AEMD and NEMD.

IV. PHONON TRANSPORT MECHANISM

Due to the fact that MD tracks atomic trajectories in the real space, it is difficult to directly extract the phonon transport mechanism. Instead, the phonon Boltzmann transport equation can be utilized to model phonon transport from the ballistic to diffusive regime [37,60–63]. In our previous work, by unifying steady-state mode-resolved BTE ("steady-state BTE") and NEMD, we showed that the physics of size-dependent thermal conductivity in NEMD is due to the ballistic phonon transport [21]. To understand the phonon transport mechanism in AEMD, we solve the one-dimensional (1D) transient mode-resolved phonon BTE ("transient BTE") under the relaxation time approximation (RTA). In order to compare the BTE and AEMD quantitatively, phonon transport parameters in crystal silicon at 300 K with the Tersoff potential are extracted from lattice dynamics [64,65]. The transient BTE and lattice dynamics calculation details can be found in Appendix B.

Comparing size-dependent thermal conductivity in the transient BTE and AEMD from 10 to 1100 nm in Fig. 3(a), we find an agreement of the thermal conductivity in the two methods, with a maximum difference of 14%. The difference is possibly due to the RTA in the BTE model [66,67]. Due to the lower computational cost of BTE, we further calculate the thermal conductivity of the entire ballistic to diffusive regime using BTE, with similar settings as the AEMD and NEMD simulations.

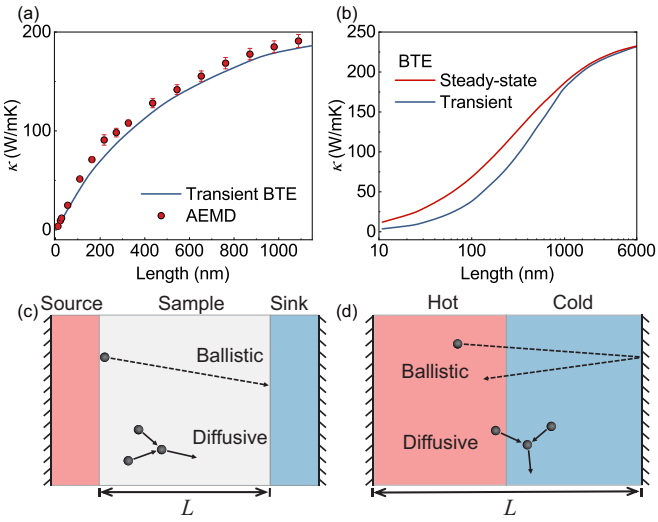

FIG. 3. (a) Thermal conductivity in AEMD and transient BTE from 10 to 1100 nm. The red dots represent the AEMD results and the blue line represents the BTE results. (b) Comparison of size-dependent thermal conductivity in steady-state and transient BTE from 10 nm to 6 μm. The blue and red lines represent the steady-state BTE and transient BTE, respectively. (c) Schematic diagram of diffusive and ballistic phonon transport in NEMD. The trajectories of ballistic transport and diffusive transport are represented by dashed lines and solid lines, respectively. In NEMD, phonons of ballistic transport emitted from the heat source are absorbed by the heat sink and contribute to the thermal conductivity. (d) Schematic diagram of diffusive and ballistic phonon transport in AEMD. Some phonons of ballistic transport emitted from the hot block bounce back to the hot block without scattering with other phonons, which does not contribute to the thermal conductivity.

The size-dependent thermal conductivities in steady-state BTE and transient BTE sampled from 10 nm to 6 μm are shown in Fig. 3(b). At 6 μm, the obtained thermal conductivity in transient BTE is 231.8 W/mK, which is close to 232.5 W/mK in steady-state BTE. The consistency is due to the identical phonon behavior in the two methods at the diffusive limit, when Fourier's law is valid.

The relative difference of thermal conductivity increases with decreasing size. For example, at 6 μm the ratio of thermal conductivity values in transient BTE over that in steady-state BTE is 0.99. However, the ratio is 0.57 at 109 nm and is only 0.30 at 11 nm. It indicates that the phonon transport mechanisms in the two methods are not identical under the limited size. When the length of the system is comparable to a phonon mean-free path, the phonon experiences ballistic transport. Figure 3(c) shows the typical phonon transport process in NEMD. The phonons emitted from the heat source move through the simulation domain and are eventually absorbed by the heat sink. Those phonons with large mean-free paths may directly transport from the heat source to the heat sink without scattering, which contributes to heat flux. In comparison, in AEMD, a phonon with large mean-free path generated from the hot block can move through the cold block, and returns to the hot block by specular reflection at the boundary, as shown in Fig. 3(d). Therefore, some phonons with large mean-free paths in AEMD do not contribute to the heat flux. This explains why the thermal conductivity in AEMD is smaller than that in NEMD with the same size. When the simulation length increases, phonons have a smaller probability of ballistic transport, and the difference is becoming smaller and eventually diminishes at the diffusive limit. Based on the above considerations, we can draw the following conclusions. First, the size effect of AEMD also originates from ballistic phonon transport. Second, the different size-dependent thermal conductivities between AEMD and NEMD simulation are due to the different contributions of the ballistic phonon transport.

TABLE I. Proportion of different phonons in MC simulations.

Simulation size (nm)	Ballistic phonons (%)	Ballistic phonons with no contribution to κ (%)
100	68.8	34.7
500	6.6	27.8

To provide a simple demonstration of the phonon transport behavior in AEMD, we simulate the phonon transport in crystal silicon with the Tersoff potential using the simplified gray model with 1D phonon Monte Carlo (MC) simulation [68–70]. The mean-free path is set as 142 nm, which is averaged from all phonon bands in BTE. The MC simulations have been validated with the analytical solution of gray BTE [37,71]. The chosen simulation sizes are 100 and 500 nm with the same boundary conditions and initial conditions as our AEMD simulations. We simulate the process from the initial state to the state where the average temperature difference between the hot block and cold block is 20 K. The simulation time is 22 ps in the 100-nm domain and 151 ps in the 500-nm domain. During the simulation process, if a phonon does not experience any scattering, it is called a ballistic phonon. As shown in Table I, it is found that the proportion of ballistic phonons decreases with increasing simulation size, from 68.8 to 6.6%. Among the ballistic phonons, we count the number of phonons whose initial and final positions are both in the hot block. These phonons do not contribute to the thermal conductivity (κ). Their proportion decreases with increasing size, from 34.7 to 27.8%. The results corroborate our conclusion that the size effect in AEMD originates from ballistic phonon transport.

V. DISCUSSION

Based on the equivalence of AEMD and the mode-resolved transient BTE, transient BTE can replace AEMD to obtain the size-dependent thermal conductivity in the same process. Recently, Hua *et al.* [72] derived the analytical expression of mode-level phonon heat flux related to temperature gradient, boundary condition, and heat generation from transient BTE with the RTA. The analytical expression provides a relationship between thermal conductivity and simulation size. Following this work, we derive an expression for AEMD to extrapolate the bulk thermal conductivity,

$$\kappa(L) = \frac{\kappa_1}{1+\frac{4\pi^2\Lambda_1^2}{L^2}} + \frac{\kappa_2}{1+\frac{4\pi^2\Lambda_2^2}{L^2}}, \tag{4}$$

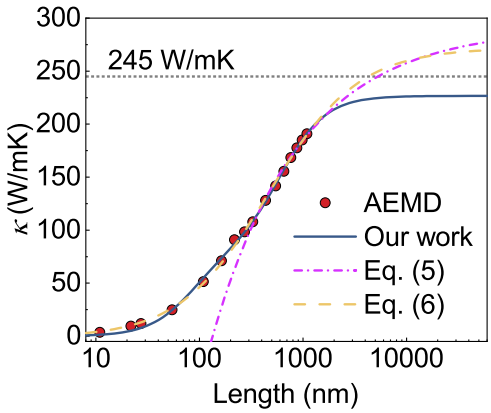

FIG. 4. Comparison of different extrapolation formulas fitting the AEMD results. The red dots represent the AEMD results. The blue solid line represents the formula in Eq. (4). The purple dotted-dashed line represents the formula in Eq. (5). The yellow dashed line represents the formula in Eq. (6). The gray dotted line represents the bulk thermal conductivity from NEMD. It can be seen intuitively that the extrapolation result from our work is the closest to the reference result.

where κ_1, κ_2, Λ_1, and Λ_2 are unknown parameters. Λ_1 and Λ_2 are associated with phonon mean-free path and the extrapolated bulk thermal conductivity is represented by $\kappa_{\text{bulk}} = \kappa_1 + \kappa_2$. The unknown parameters are determined by fitting the AEMD results. Detailed derivations are provided in Appendix C.

In Fig. 4, the bulk thermal conductivity of crystal silicon at 300 K is obtained by fitting the AEMD data with Eq. (4) (blue solid lines). The extrapolated thermal conductivity value is 227 ± 24 W/mK (within a 95% confidence interval), which is almost consistent with the bulk thermal conductivity 245 W/mK from NEMD [21]. We also compare our method with methods used in previous studies. Equation (5) is raised by Zaoui *et al.* [34]:

$$\kappa(L) = \kappa_{\text{bulk}}\left(1 - \sqrt{\frac{\Lambda_0}{L}}\right), \tag{5}$$

where L is the simulation length and Λ_0 is an unknown parameter related to phonon mean-free paths. Another extrapolation method proposed by Sellan *et al.* [30] was initially proposed for NEMD extrapolation, but later also adopted in AEMD extrapolation [34]:

$$\kappa(L) = \kappa_{\text{bulk}}\Big/\left(1 + \frac{a_1}{L} + \frac{1}{2}\left(\frac{a_2}{L}\right)^2\right), \tag{6}$$

where a_1 and a_2 are the unknown parameters to be determined in the fitting process.

The fitting curves from Eq. (5) and Eq. (6) can also be found in Fig. (4). Equation (5) is approximately consistent with the AEMD results when the simulation length is larger than 200 nm, but a significant difference appears in the ballistic regime. The extrapolated thermal conductivity is 288 ± 25 W/mK, which is larger than 245 W/mK. Equation (6) seems to also match the AEMD data well in the samples of length from 10 to 1100 nm. However, this is a mathematical coincidence. If larger sizes are considered, Eq. (6) does not match the BTE-predicted thermal conductivity values well. These data are not shown here for brevity. Moreover, the extrapolated thermal conductivity is 273 ± 13 W/mK, which is also larger than the result from NEMD.

To ensure the accuracy of our extrapolation, we recommend that the simulation size range is from 1 to 6× the average mean-free paths. For silicon with the Tersoff potential, whose average mean-free path is 142 nm, the recommended size range for extrapolation is from 150 to 900 nm, which has a reasonable computational cost. The extrapolated thermal conductivity is 242 ± 30 W/mK (within a 95% confidence interval) and almost the same as the result from NEMD. Using data from smaller domain sizes will affect the results of the extrapolation [51], while using data from lager domain sizes will not further improve the extrapolation result and will unnecessarily increase the computational cost.

VI. CONCLUSION

In this paper, we investigate the thermal transport mechanism in AEMD by comparing the size-dependent thermal conductivity of AEMD, NEMD, and transient BTE, using silicon with the Tersoff potential as an example. From a comparison of AEMD and NEMD, we find a large difference between results obtained from the two methods. We demonstrate two reasons for this difference. The first is the mismatched direction of heat flux between the two methods. By adopting the fixed boundary to replace the periodic boundary in AEMD and reducing the size to one-half of the original one, we unify the direction of heat flux in AEMD and NEMD and narrow the difference of size effect between AEMD and NEMD. The second is the different thermal transport mechanism. By comparing the AEMD and transient BTE, we reveal that the phonon transport mechanism that leads to the size-dependent thermal conductivity in AEMD is ballistic phonon transport. Nevertheless, the mechanism is not completely the same as in NEMD, because some phonons with long mean-free paths do not contribute to the heat conduction. Based on this understanding, we propose an extrapolation method for AEMD which performs better than other extrapolation methods. The extrapolated thermal conductivity of the Tersoff silicon is 242 ± 30 (W/mK), which is almost identical to the bulk value. We recommend using simulation data from 1 to 6× the average mean-free path, which will improve the extrapolation results. The understanding of AEMD not only benefits for future MD simulations, but also helps researchers to better appreciate the differences between steady state and transient thermal transport at nanoscale.

ACKNOWLEDGMENTS

Y.S., Y.H., and H.B. acknowledge the support by the National Natural Science Foundation of China (Grant No. 52122606). Z.F. acknowledges the support from the National Natural Science Foundation of China (Grant No. 11974059). The numerical simulations were carried out on the π 2.0 cluster supported by the Center for High Performance Computing at Shanghai Jiao Tong University.

APPENDIX A: DETAILED PROCESS OF AEMD SIMULATION

In this section, we show the AEMD and NEMD calculations in detail. For AEMD simulation, in all three directions of the simulation domain, the boundaries are set as periodic. The cross section is set as 16×16 silicon supercells to mimic an infinitely large cross section after a convergence test. The time step of the whole simulation is 1 fs to resolve all the phonon frequencies. Initially, the simulation domain is set under an NPT ensemble (constant mass, pressure, and temperature) to relax the system from 50 ps to 1 ns depending on the simulation domain. Then, the system is divided into hot block and cold block, each part heated under 320 and 280 K, respectively, with Nosé-Hoover chain thermostats for 50 ps until the step-difference temperature distribution is established. Subsequently, the whole system converts to the NVE ensemble (constant mass, volume, and energy). In the NVE ensemble, the temperature distribution along the x axis is sampled every 4000 steps until the system gradually returns to equilibrium. One can then obtain the thermal conductivity of the sample by fitting the decay curve of the average temperature difference between the hot block and cold block with the solution of the heat diffusion equation.

For NEMD simulations, in the transport direction, two fixed layers of silicon supercells are placed at the boundaries. Heat source region and heat sink region are divided at both ends of the simulation domain. The cross section is set as periodic boundaries with 8×8 silicon supercells to mimic an infinitely large cross section after a convergence test. The time step of the whole simulation is 1 fs. The whole system is initially relaxed under the NPT ensemble for 1 ns. Then, the Langevin thermostats are applied to the heat source and the heat sink regions, 320 and 280 K, respectively. The simulation domain is set under the NVE ensemble for 20 ns. In the last 5 ns, the energy deposited to the heat source and energy extracted from the heat sink are averaged to calculate the transferred energy ΔE, and the heat flux q is calculated by [29,51]

$$q = \Delta E/(S\Delta t), \tag{A1}$$

where $\Delta E/\Delta t$ is the energy transfer rate and S is the cross-sectional area perpendicular to the x axis. The NEMD simulation method has been well discussed by Hu *et al.* [21].

APPENDIX B: DETAILED SETTINGS OF TRANSIENT BTE

The 1D transient BTE with RTA [73] is given by

$$\frac{\partial g_\mu(x,\,t)}{\partial t} + \mathrm{v}_\mu \nabla g_\mu(x,\,t) = -\frac{g_\mu(x,\,t) - g_0(T(x,\,t))}{\tau_\mu}, \tag{B1}$$

where $g_\mu(x,\,t)$ is the deviational energy distribution from the given equilibrium at position x and time t for a certain phonon mode μ (frequency ω_μ and polarization p), and τ_μ is the phonon relaxation time. $g_0(T(x,\,t)) = \frac{1}{4\pi} C_\mu (T - T_0)$ is the equilibrium energy distribution at a certain temperature T, where C_μ is the heat capacity per unit volume and T_0 is the reference temperature, 300 K. The transient BTE is numerically solved by the finite-volume method [74]. The specular boundary condition is set to simulate the fixed boundary in AEMD [21]. The initial condition settings are also the same as AEMD. All the results in transient BTE are obtained after convergence tests on the time step, number of meshes, number of angles, and number of phonon bands. In order to compare the BTE and AEMD quantitatively, phonon transport parameters in the crystal silicon at 300 K with the Tersoff potential are extracted from harmonic and third-order anharmonic lattice dynamics [64,65], including the group velocity v_μ, the relaxation time τ_μ, and the heat capacity C_μ for every phonon mode. Considering the computational cost, phonon modes are integrated into sufficient phonon bands after convergence tests. It is worth mentioning that the phonons should follow the Bose-Einstein distribution $f_0(T) = \frac{1}{e^{(\hbar\omega)/(k_B T)} - 1}$ [75]. However, in MD simulations, since all phonon modes have been excited, the phonons follow the classical Maxwell-Boltzmann distribution $f_0^{MB}(T) = e^{-[(\hbar\omega)/(k_B T)]}$ [65]. One can decrease the Planck constant $\hbar$ in the Bose-Einstein distribution to approach the classical limit [65]. The details of anharmonic lattice dynamics can be found in previous studies [21,65,76,77].

APPENDIX C: DERIVATION OF EXTRAPOLATION FORMULA

Hua *et al.* [72] derive the "generalized Fourier law" from the mode-level transient BTE with RTA. To make it easier for readers, we first repeat the derivation. It starts with

$$\frac{\partial g_\mu(\mathbf{x},\,t)}{\partial t} + \mathbf{v}_\mu \cdot \nabla g_\mu(\mathbf{x},\,t) = -\frac{g_\mu(\mathbf{x},\,t) - g_0(T(\mathbf{x},\,t))}{\tau_\mu} + Q_\mu(\mathbf{x},\,t), \tag{C1}$$

where $g_\mu(\mathbf{x},\,t) = \hbar\omega_\mu[f_\mu(\mathbf{x},\,t) - f_0(T_0)]$ is the deviational energy distribution from the given equilibrium at position $\mathbf{x}$ and time t for a certain phonon mode μ (frequency ω_μ), τ_μ is the phonon relaxation time, and Q_μ is the heat generation term. $g_0(T(\mathbf{x},\,t))$ is given by

$$g_0(T(\mathbf{x},\,t)) = \hbar\omega_\mu[f_0(T(\mathbf{x},\,t)) - f_0(T_0)] = C_\mu \Delta T(\mathbf{x},\,t), \tag{C2}$$

where T_0 is the given equilibrium temperature, ΔT is the temperature derivation from the equilibrium, and C_μ is phonon mode-level heat capacity which does not change with temperature. In order to describe the transport process in our AEMD simulation, only one direction needs to be considered. A Fourier transform in time t is performed on Eq. (C1):

$$\Lambda_{\mu x}\frac{\partial \tilde{g}_\mu}{\partial x} + (1 + i\eta\tau_\mu)\tilde{g}_\mu = C_\mu \Delta\tilde{T} + \tilde{Q}_\mu \tau_\mu, \tag{C3}$$

where η is the Fourier temporal frequency and $\Lambda_{\mu x}$ is the phonon mean-free path along the x direction. Equation (C3) is a first-order partial differential equation which can be solved by integration to get the expression of $\tilde{g}_\mu(x,\,\eta)$. The mode-level heat flux $\tilde{q}_{\mu x} = \upsilon_{\mu x}\tilde{g}_\mu$ along the x direction is

$$\tilde{q}_{\mu x} = -\int_\Gamma C_\mu \upsilon_{\mu x}\Lambda_{\mu x}\frac{e^{-(1+i\eta\tau_\mu)|(x-x')/\Lambda_{\mu x}|}}{(1 + i\eta\tau_\mu)|\Lambda_{\mu x}|}\frac{\partial\tilde{T}}{\partial x'}dx' + \int_\Gamma \tilde{Q}_\mu(x')e^{-(1+i\eta\tau_\mu)|(x-x')/\Lambda_{\mu x}|}dx', \tag{C4}$$

where

$$\Gamma \in \begin{cases} (-\infty,\ x) & \text{if } \upsilon_{\mu x} > 0, \\ (x,\ \infty) & \text{if } \upsilon_{\mu x} > 0. \end{cases}$$

It is assumed the temperature profile has a spatial dependence of $e^{i\zeta x}$. $\zeta = 2\pi/L$, L is the simulation length. Based on the derivations above, we find that the usage scenario of Eq. (C4) is completely the same as AEMD if the thermal excitation is not considered (the complete derivation can be found in Ref. [72]),

$$\tilde{q}(x,\ \eta) = i\zeta \tilde{T}(\eta) e^{i\zeta x} \sum_{\mu} \frac{\kappa_\mu}{1 + {\Lambda_\mu}^2 \zeta^2}. \tag{C5}$$

Equation (C5) degenerates into Fourier's law when the simulation length approaches the diffusive limit. In this way, $q = -\kappa \frac{\partial T}{\partial x}$, which agrees with Eq. (C5) if we define the thermal conductivity

$$\kappa = \sum_{\mu} \frac{\kappa_\mu}{1 + \Lambda_\mu^2 \zeta^2} \tag{C6}$$

In Eq. (C6), the apparent thermal conductivity is related to mode-level phonon mean-free path Λ_μ, thermal conductivity κ_μ, and the simulation size. This formula is based on the same phonon transport mechanism as AEMD and can be used as a fitting formula to extrapolate bulk thermal conductivity from finite-size thermal conductivity. Lack of phonon information in the AEMD simulation, the thermal conductivity of a certain phonon mode κ_μ, and phonon mean-free path Λ_μ are treated as fitting parameters in our extrapolation. It is verified that the more phonon modes are selected, the more accurate the result will be. However, the number of fitting parameters increases with the selected phonon modes, which leads to larger uncertainty. To balance accuracy and certainty, we choose two phonon modes and the extrapolation formula is

$$\kappa(L) = \frac{\kappa_1}{1 + \frac{4\pi^2 \Lambda_1^2}{L^2}} + \frac{\kappa_2}{1 + \frac{4\pi^2 \Lambda_2^2}{L^2}} \tag{C7}$$

This is the formula used in the main text of the paper.

[1] A. Berker, S. Chynoweth, U. C. Klomp, and Y. Michopoulos, J. Chem. Soc. Faraday Trans. **88**, 1719 (1992).
[2] T. Ikeshoji and B. Hafskjold, Mol. Phys. **81**, 251 (1994).
[3] F. Müller-Plathe, J. Chem. Phys. **106**, 6082 (1997).
[4] A. J. H. McGaughey and M. Kaviany, Int. J. Heat Mass Transfer **47**, 1799 (2004).
[5] Z. Fan, L. F. C. Pereira, H.-Q. Wang, J.-C. Zheng, D. Donadio, and A. Harju, Phys. Rev. B **92**, 094301 (2015).
[6] T. Feng, W. Yao, Z. Wang, J. Shi, C. Li, B. Cao, and X. Ruan, Phys. Rev. B **95**, 195202 (2017).
[7] H. Bao, J. Chen, X. Gu, and B. Cao, ES Energy Environ. **1**, 16 (2018).
[8] Z. Liang and P. Keblinski, J. Chem. Phys. **148**, 064708 (2018).
[9] T.-Q. Duong, C. Massobrio, G. Ori, M. Boero, and E. Martin, Phys. Rev Mater. **3**, 105401 (2019).
[10] X. Gu, Z. Fan, and H. Bao, J. Appl. Phys. **130**, 210902 (2021).
[11] J. W. Che, T. Cagin, W. Q. Deng, and W. A. Goddard, J. Chem. Phys. **113**, 6888 (2000).
[12] H. Dong, S. Xiong, Z. Fan, P. Qian, Y. Su, and T. Ala-Nissila, Phys. Rev. B **103**, 035417 (2021).
[13] M. S. Green, J. Chem. Phys. **22**, 398 (1954).
[14] R. Kubo, J. Phys. Soc. Jpn. **12**, 570 (1957).
[15] J. Chen, G. Zhang, and B. Li, Phys. Lett. A **374**, 2392 (2010).
[16] W. J. Evans, L. Hu, and P. Keblinski, Appl. Phys. Lett. **96**, 203112 (2010).
[17] Y. Chen, D. Li, J. R. Lukes, Z. Ni, and M. Chen, Phys. Rev. B **72**, 174302 (2005).
[18] Y. Wang, X. Ruan, and A. K. Roy, Phys. Rev. B **85**, 205311 (2012).
[19] Z. Lu, Y. Wang, and X. Ruan, Phys. Rev. B **93**, 064302 (2016).
[20] Z. Li, S. Xiong, C. Sievers, Y. Hu, Z. Fan, N. Wei, H. Bao, S. Chen, D. Donadio, and T. Ala-Nissila, J. Chem. Phys. **151**, 234105 (2019).
[21] Y. Hu, T. Feng, X. Gu, Z. Fan, X. Wang, M. Lundstrom, S. S. Shrestha, and H. Bao, Phys. Rev. B **101**, 155308 (2020).
[22] I. Jang, S. B. Sinnott, D. Danailov, and P. Keblinski, Nano Lett. **4**, 109 (2004).
[23] A. J. McGaughey and M. Kaviany, Adv. Heat Transfer **39**, 169 (2006).
[24] J. Shiomi and S. Maruyama, Phys. Rev. B **73**, 205420 (2006).
[25] N. A. Roberts, D. Walker, and D. Li, Int. J. Heat Mass Transfer **52**, 2002 (2009).
[26] T. Luo, K. Esfarjani, J. Shiomi, A. Henry, and G. Chen, J. Appl. Phys. **109**, 074321 (2011).
[27] T. Hori, T. Shiga, and J. Shiomi, J. Appl. Phys. **113**, 203514 (2013).
[28] Z. Liang, W. Evans, and P. Keblinski, Phys. Rev. E **87**, 022119 (2013).
[29] P. K. Schelling, S. R. Phillpot, and P. Keblinski, Phys. Rev. B **65**, 144306 (2002).
[30] D. P. Sellan, E. S. Landry, J. E. Turney, A. J. H. McGaughey, and C. H. Amon, Phys. Rev. B **81**, 214305 (2010).
[31] Z. Wang and X. Ruan, J. Appl. Phys. **121**, 044301 (2017).
[32] E. Lampin, P. L. Palla, P. A. Francioso, and F. Cleri, J. Appl. Phys. **114**, 033525 (2013).
[33] C. Melis, R. Dettori, S. Vandermeulen, and L. Colombo, Eur. Phys. J. B **87**, 96 (2014).
[34] H. Zaoui, P. L. Palla, F. Cleri, and E. Lampin, Phys. Rev. B **94**, 054304 (2016).
[35] G. Fugallo and L. Colombo, Phys. Scr. **93**, 043002 (2018).
[36] A. A. Maznev, J. A. Johnson, and K. A. Nelson, Phys. Rev. B **84**, 195206 (2011).
[37] K. C. Collins, A. A. Maznev, Z. Tian, K. Esfarjani, K. A. Nelson, and G. Chen, J. Appl. Phys. **114**, 104302 (2013).
[38] J. A. Johnson, A. A. Maznev, J. Cuffe, J. K. Eliason, A. J. Minnich, T. Kehoe, C. M. Sotomayor Torres, G. Chen, and K. A. Nelson, Phys. Rev. Lett. **110**, 025901 (2013).
[39] M. G. Muraleedharan, K. Gordiz, A. Rohskopf, S. T. Wyant, Z. Cheng, S. Graham, and A. Henry, arXiv:2011.01070 (2020).
[40] G. Barbarino, C. Melis, and L. Colombo, Carbon **80**, 167 (2014).
[41] G. Barbarino, C. Melis, and L. Colombo, Phys. Rev. B **91**, 035416 (2015).

[42] K. R. Hahn, M. Puligheddu, and L. Colombo, Phys. Rev. B **91**, 195313 (2015).
[43] P. L. Palla, S. Zampa, E. Martin, and F. Cleri, Int. J. Heat Mass Transfer **131**, 932 (2019).
[44] R. Dettori, C. Melis, X. Cartoixà, R. Rurali, and L. Colombo, Phys. Rev. B **91**, 054305 (2015).
[45] X. Cartoixà, R. Dettori, C. Melis, L. Colombo, and R. Rurali, Appl. Phys. Lett. **109**, 013107 (2016).
[46] A. Crnjar, C. Melis, and L. Colombo, Phys. Rev. Mater. **2**, 015603 (2018).
[47] A. Cappai, A. Antidormi, A. Bosin, D. Narducci, L. Colombo, and C. Melis, Phys. Rev. Mater. **4**, 035401 (2020).
[48] M. Puligheddu, F. Gygi, and G. Galli, Phys. Rev. Mater. **1**, 060802(R) (2017).
[49] Z. Zeng, C. Zhang, Y. Xia, Z. Fan, C. Wolverton, and Y. Chen, Phys. Rev. B **103**, 224307 (2021).
[50] P. C. Howell, J. Chem. Phys. **137**, 224111 (2012).
[51] H. Dong, Z. Fan, L. Shi, A. Harju, and T. Ala-Nissila, Phys. Rev. B **97**, 094305 (2018).
[52] D. J. Evans, Phys. Lett. A **91**, 457 (1982).
[53] J. R. Lukes and H. Zhong, J. Heat Transfer **129**, 705 (2007).
[54] K. K. Mandadapu, R. E. Jones, and P. Papadopoulos, J. Chem. Phys. **130**, 204106 (2009).
[55] Z. Fan, H. Dong, A. Harju, and T. Ala-Nissila, Phys. Rev. B **99**, 064308 (2019).
[56] K. Xu, A. J. Gabourie, A. Hashemi, Z. Fan, N. Wei, A. B. Farimani, H.-P. Komsa, A. V. Krasheninnikov, E. Pop, and T. Ala-Nissila, Phys. Rev. B **99**, 054303 (2019).
[57] Z. Rashid, L. Zhu, and W. Li, Phys. Rev. B **97**, 075441 (2018).
[58] J. Tersoff, Phys. Rev. B: Condens. Matter **39**, 5566 (1989).
[59] S. Plimpton, J. Comput. Phys. **117**, 1 (1995).
[60] D. Donadio and G. Galli, Phys. Rev. Lett. **99**, 255502 (2007).
[61] A. J. Minnich, G. Chen, S. Mansoor, and B. S. Yilbas, Phys. Rev. B **84**, 235207 (2011).
[62] C. Hua and A. J. Minnich, Phys. Rev. B **89**, 094302 (2014).
[63] A. J. Minnich, J. Phys.: Condens. Matter **27**, 053202 (2015).
[64] Z. Tong and H. Bao, Int. J. Heat Mass Transfer **117**, 972 (2018).
[65] X. Gu, Z. Fan, H. Bao, and C. Y. Zhao, Phys. Rev. B **100**, 064306 (2019).
[66] A. Ward and D. A. Broido, Phys. Rev. B **81**, 085205 (2010).
[67] J. G. Christenson, M. P. Kroonblawd, R. A. Austin, L. E. Fried, and R. J. Phillips, Phys. Rev. B **102**, 205406 (2020).
[68] S. Mazumder and A. Majumdar, J. Heat Transfer **123**, 749 (2001).
[69] Y. F. Chen, D. Y. Li, J. R. Lukes, and A. Majumdar, J. Heat Transfer **127**, 1129 (2005).
[70] D. Lacroix, K. Joulain, and D. Lemonnier, Phys. Rev. B **72**, 064305 (2005).
[71] Z. Guo and K. Xu, Int. J. Heat Mass Transfer **102**, 944 (2016).
[72] C. Hua, L. Lindsay, X. Chen, and A. J. Minnich, Phys. Rev. B **100**, 085203 (2019).
[73] S. Zahiri, Z. Xu, Y. Hu, H. Bao, and Y. X. Shen, Int. J. Heat Mass Transfer **138**, 267 (2019).
[74] S. A. Ali, G. Kollu, S. Mazumder, P. Sadayappan, and A. Mittal, Int. J. Therm. Sci. **86**, 341 (2014).
[75] S. J. Blundell and K. M. Blundell, *Concepts in Thermal Physics* (Oxford University Press, Oxford, 2009).
[76] F. Barocchi, M. Neumann, and M. Zoppi, Phys. Rev. A: Gen. Phys. **36**, 2440 (1987).
[77] H. Xie, X. Gu, and H. Bao, Comput. Mater. Sci. **138**, 368 (2017).